Overview of Physics Results from MAST

B. Lloyd[1], R.J. Akers[1], F. Alladio[2], S. Allan[1], L.C. Appel[1], M. Barnes[1,3], N.C. Barratt[4], N. Ben Ayed[1], B.N. Breizman[5], M. Cecconello[6], C.D. Challis[1], I.T. Chapman[1], D. Ciric[1], G. Colyer[1], J.W. Connor[1], N.J. Conway[1], M. Cox[1], S.C. Cowley[1], G. Cunningham[1], A. Darke[1], M. De Bock[1], E. Delchambre[7], G. De Temmerman[1], R.O. Dendy[1], P. Denner[4], M.D. Driscoll[1], B. Dudson[4], D. Dunai[8], M. Dunstan[1], S. Elmore[9], A.R. Field[1], G. Fishpool[1], S. Freethy[4], L. Garzotti[1], K.J. Gibson[4], M.P. Gryaznevich[1], W. Guttenfelder[10], J Harrison[1,4], R.J. Hastie[1], N.C. Hawkes[1], T.C. Hender[1], B. Hnat[10], D.F. Howell[1], M-D Hua[11], A. Hubbard[12], G. Huysmans[7], D. Keeling[1], Y.C. Kim[3], A. Kirk[1], Y. Liang[13], M.K. Lilley[14], M. Lisak[14], S. Lisgo[1], Y.Q. Liu[1], G.P. Maddison[1], R. Maingi[15], S.J. Manhood[1], R. Martin[1], G.J. McArdle[1], J. McCone[16], H. Meyer[1], C. Michael[1], S. Mordijck[17], T. Morgan[4], A.W. Morris[1], D.G. Muir[1], E. Nardon[1], G. Naylor[1], M.R. O'Brien[1], T. O'Gorman[16], J. Páleník[18], A. Patel[1], S.D. Pinches[1], M.N. Price[1], C.M. Roach[1], V. Rozhansky[19], S. Saarelma[1], S.A. Sabbagh[20], A. Saveliev[21], R. Scannell[1], S.E. Sharapov[1], V. Shevchenko[1], S. Shibaev[1], D. Stork[1], J. Storrs[1], W. Suttrop[22], A. Sykes[1], P. Tamain[1], D. Taylor[1], D. Temple[11], N. Thomas-Davies[1], A. Thornton[4], M.R. Turnyanskiy[1], M. Valovic[1], R.G.L. Vann[4], G. Voss[1], M.J. Walsh[1], S.E.V. Warder[1], H.R. Wilson[4], M. Windridge[11], M Wisse[1], S. Zoletnik[8] and the MAST and NBI teams.

[1]EURATOM/CCFE Fusion Association, Culham Science Centre, Abingdon, UK
[2]Associazione EURATOM-ENEA sulla Fusione, Frascati, Rome, Italy
[3]Rudolf Peierls Centre for Theoretical Physics, University of Oxford, Oxford, UK.
[4]University of York, Heslington, York, UK
[5]Institute for Fusion Studies, University of Texas, Austin, Texas, 78712 USA
[6]EURATOM-VR Association, Uppsala University, SE-75120 Uppsala, Sweden
[7]CEA-Cadarache, Association Euratom-CEA, 13108 St Paul-lez-Durance, France
[8]KFKI-RMKI, Association EURATOM, Pf. 49, H-1525 Budapest, Hungary
[9]University of Liverpool, Brownlow Hill, Liverpool, UK
[10]Department of Physics, Warwick University, UK.
[11]Imperial College of Science, Technology and Medicine, London, UK.
[12]MIT Plasma Science and Fusion Center, Cambridge, MA 02139, USA
[13]Association EURATOM-FZ Jülich, Trilateral Euregio Cluster, D-52425 Jülich, Germany
[14]Chalmers University of Technology, 41296 Göteborg, Sweden
[15]Oak Ridge National Laboratory, Oak Ridge, USA.
[16]University College, Cork, Association EURATOM-DCU Ireland.
[17]University of California-San Diego, 9500 Gilman Dr, La Jolla, California 92093, USA
[18]Association EURATOM Comenius University, Slovakia
[19]St. Petersburg State Polytechnical University, St. Petersburg, Russia.
[20]Dept of Applied Physics and Applied Maths, Columbia University, New York, NY, USA
[21]A.F. Ioffe Physico-Technical Institute, St. Petersburg, Russia.
[22]Max-Planck-Institut für Plasmaphysik, EURATOM Association, Garching, Germany
e-mail contact of main author: brian.lloyd@ccfe.ac.uk

Abstract. Major plant and diagnostic developments on MAST have enabled important advances in support of ITER, definition of a component test facility (CTF) and the clarification of underlying tokamak physics. For example, L-H transition studies benefit from high spatial and temporal resolution measurements of pedestal profile evolution (temperature, density and radial electric field) and in support of pedestal stability studies the edge current density profile has been determined from Motional Stark Effect (MSE) measurements. The influence of the q-profile and E×B flow shear on transport has been studied in MAST and equilibrium flow shear has been included in gyro-kinetic codes, improving comparisons with the experimental data. H-modes exhibit a

weaker q and stronger collisionality dependence of heat diffusivity than implied by IPB98(y,2) scaling, which may have important implications for the design of an ST-based CTF. ELM mitigation, an important issue for ITER, has been demonstrated by applying resonant magnetic perturbations (RMPs) using both internal and external coils, but full stabilization of type I ELMs has not been observed. Modelling shows the importance of including the plasma response to the RMP fields. MAST plasmas with q > 1 and weak central magnetic shear regularly exhibit a long-lived saturated ideal internal mode. Measured plasma braking in the presence of this mode compares well with neoclassical toroidal viscosity theory. In support of basic physics understanding, high resolution Thomson scattering measurements are providing new insight into sawtooth crash dynamics and neoclassical tearing mode critical island widths. Retarding Field Analyzer measurements show elevated ion temperatures in the scrape-off layer of L-mode plasmas and, in the presence of type I ELMs, ions with energy greater than 500eV are detected 20cm outside the separatrix. Disruption mitigation by massive gas injection has reduced divertor heat loads by up to 70 per cent.

1. Introduction

The Mega Amp Spherical Tokamak (MAST) is designed to study low aspect ratio (R/a ~ 0.85m/0.65m ~ 1.3), highly elongated ($\kappa > 2$), plasmas ($I_p \leq 1.5MA$, $B_t \leq 0.52T$) at high ion and electron temperature. It is equipped with high power neutral beam heating, adaptable fuelling systems including pellet injection, digital plasma control, error field compensation coils and a comprehensive range of high resolution diagnostics. The physics programme comprises three main elements: (i) exploring the long term potential of the spherical tokamak as a fusion Component Test Facility (CTF) and/or an advanced power plant; (ii) advancing key tokamak physics for optimal exploitation of ITER and DEMO design optimisation; and (iii) providing unique insight into underlying tokamak physics. In pursuit of these aims, MAST capabilities have recently been further enhanced: internal ELM control coils; Toroidal Alfvén Eigenmode (TAE) excitation system; disruption mitigation system (fast gas valve on loan from FZ Jülich); divertor science facility (manipulator allowing insertion of material samples into the divertor); 28GHz gyrotron (on loan from ORNL, USA); multi-chord motional Stark effect (MSE) diagnostic; upgraded Thomson scattering (TS) system (part funded by University of York) giving very high spatial and temporal resolution together with a new triggering system allowing synchronisation to fast plasma events; collimated neutron emission detector (collaboration with Uppsala University, Sweden); and many other diagnostic developments including long wavelength infra-red imaging and a retarding field energy analyzer (on loan from CEA Cadarache). These technical developments have allowed important advances to be made on a wide range of studies in support of ITER and future STs. Results are summarised in sections 2 – 6. Future plans, which include major upgrades to MAST, are summarised in section 7.

2. Plasma Stability

2.1. Macroscopic Stability

Macroscopic stability studies, aided by high resolution diagnostics including MSE, have allowed improved understanding of performance limiting instabilities in high beta plasmas [1]. For example, MAST plasmas with q > 1 and weakly reversed magnetic shear, or broad low shear regions, regularly exhibit frequency sweeping n = 1 modes that evolve into a long-lived mode (LLM). This has been identified as a saturated ideal internal MHD instability, growing unstable as q_{min} approaches unity [2]. Higher-n modes become progressively more unstable at sufficiently small Δq (= $q_{min} - 1$). Theoretical studies have shown that the stability of the internal kink mode is highly sensitive to variations in the plasma density and rotation profiles [3,4]. The ideal internal mode results in strong braking of the core plasma, enhanced fast ion losses and degradation of the energy confinement (Fig. 1). Once Δq becomes sufficiently small that the LLM becomes unstable, the enhanced fast ion losses mean that there are no longer sufficient energetic ions within the core of the plasma to drive the 'fishbone'

instabilities and the chirping activity ceases. The measured plasma braking (by high resolution charge exchange recombination spectroscopy) due to the LLM compares favourably with neoclassical toroidal viscosity (NTV) theory [5]. External magnetic perturbations (n = 2) have also been applied in co- and counter-NBI heated plasmas to further test predictions of NTV theory. Initial analysis, for the counter-NBI case, indicates significant discrepancy between measured and predicted braking which requires additional modelling to resolve [1]. MAST plasmas have operated well above the ideal no-wall stability limit and the plasma response to externally applied non-axisymmetric magnetic fields is being measured to investigate resistive wall mode (RWM) stability for a range of fast ion distributions (achieved by varying plasma density). Both rotation and kinetic effects are important and are intricately related. Calculations for MAST show that the RWM is most unstable at intermediate densities, in qualitative agreement with experimental data. Damping is strongest at low density. At both low and high density *thermal* ion stabilisation dominates the kinetic damping of the RWM [1].

The upgraded Thomson scattering (TS) system, with radial resolution ~ 10mm and the possibility of temporal resolution ≤ 1μs, has enabled detailed analysis of the density and temperature profiles in and around a neoclassical tearing mode (NTM) island, permitting tests of models for the critical NTM island width. Initial results show that the observed threshold island width is larger than the critical width measured assuming finite parallel diffusive transport [6]. Similarly, high resolution TS measurements during the sawtooth crash have provided new insight into the crash mechanism [7]. As magnetic reconnection occurs, the growing magnetic island causes an increase in the electron temperature gradient at the island boundary layer. The island width grows and the region of increasing temperature gradient moves into a region of lower magnetic shear triggering a secondary instability, thought to be responsible for the rapidity of the collapse.
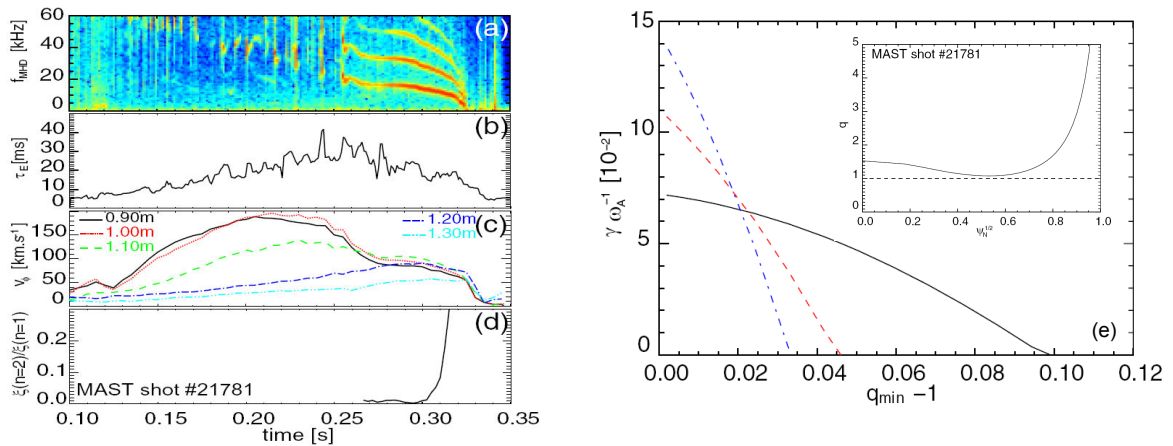

FIG 1. (a) Spectrogram of outboard magnetic probe measurements for a MAST plasma featuring the LLM, (b) energy confinement time (TRANSP), (c) plasma velocity at different major radius positions (magnetic axis at R=0.95 m), (d) amplitude ratio of the n=2 component to the n =1 component for the LLM, (e) the growth rates of the n = 1 (solid black line), n= 2 (dashed red line), and n= 3 (dash-dotted blue line) modes as a function of q_{min} at mode onset (MISHKA). Inset shows q profile at 0.22s

2.2. Current Profile Control

Current profile control is required for optimisation of plasma stability. Off-axis NBCD has been demonstrated in vertically displaced plasmas in MAST [8]. Anomalous fast ion diffusion (~ 0.5m^2/s) was invoked to explain the observed measurements. Modelling of the effects of the observed fishbone instabilities, using the non-linear HAGIS code, indicate an effective

fast ion diffusion coefficient consistent with that inferred experimentally [9]. Future studies of the impact of fast ion diffusion during current profile control experiments will benefit from installation of a new collimated neutron detector [10] and a fast ion D_α (FIDA) diagnostic. Current penetration also has an important bearing on plasma stability. The 'Ohmic' current profile evolution during the ramp-up phase of a MAST discharge has been determined from MSE measurements at the start of neutral beam injection with different NBI start times and compared with the evolution calculated by TRANSP using the earliest current profile measurements as input. Observed current penetration is significantly slower than that calculated by TRANSP using neo-classical resistivity. Further investigation is required to understand this behaviour which has also been observed in JET [11].

2.3. Fast Particle Instabilities

MAST exhibits a variety of modes excited in a broad range of frequencies from Alfvén cascade (AC) eigenmodes, toroidal Alfvén eigenmodes (TAE), and chirping modes in the frequency range 50-150 kHz, to compressional Alfvén eigenmodes (CAE) in the frequency range 0.4-3.8 MHz, which is approaching the cyclotron frequency of plasma ions. In spite of the significant differences in the nature of the modes and in the corresponding excitation mechanisms, it has been shown that the non-linear evolution of these modes is determined by the type and strength of relaxation processes of the fast particles driving the waves [12]. In particular, the disparity between experiments on AE excitation by NBI and by ICRH has been attributed to the role of dynamical friction (drag) as a relaxation process for resonant particles [13,14] in a simplified bump on tail model. HAGIS [15] modelling of Alfvénic instabilities in the presence of drag agrees with the qualitative trends of the bump on tail analysis. TAE damping is also being studied in MAST by active excitation of stable modes. So far it has proved difficult to routinely excite such modes. Studies will continue in 2011 with increased drive.

3. Confinement and Transport

3.1. Confinement Scaling

One promising application of the spherical tokamak (ST) is an intense volume neutron source for testing fusion components [16]. To predict plasma performance in such a Component Test Facility (CTF), reliable estimates of energy confinement time τ_E are required. H-mode plasmas in both MAST [17] and NSTX [18] exhibit a slightly weaker scaling of τ_E with I_p and a much stronger scaling with B_t than given by the IPB98(y,2) scaling. For example, MAST data indicate that the thermal energy confinement time $\tau_{E,th}$ scales as $\tau_{E,th} \propto I_p^{0.59} B_t^{1.4}$. Transport analysis showed that the strong B_t scaling could be explained by a weaker safety factor (q) and a stronger collisionality (ν_e^*) dependence of heat diffusivity than implied by IPB98(y,2). This interpretation has now been confirmed in MAST by dedicated scaling experiments, in which all dimensionless parameters except the one being studied are held approximately constant [19]. These studies were conducted in double null (DN) deuterium plasmas. The results indicated that $\tau_{E,th} B_t \propto \nu_e^{*-0.82\pm0.1} q^{-0.85}$ (Fig. 2), which is quantitatively consistent with the plasma current and toroidal field scaling measured earlier, assuming gyro-Bohm scaling [17]. Detailed transport analysis shows that ion transport is close to neoclassical and local heat transport is dominated by the electrons. Furthermore, for the ν_e^* scan data set, $\chi_e/B_t \propto \nu_e^{*(0.5-1)}$ consistent with the global confinement scaling, and the measured neutron rate increases strongly with toroidal magnetic field, $S_{DD} \propto B_t^{2.85}$, in good agreement with the ν_e^* scaling. In order to match the measured neutron rate in TRANSP simulations, however, it is necessary to invoke a fast ion diffusion coefficient $D_{fast} \sim 2 - 3$ m^2/s. The underlying cause

of the ν_e^* scaling is still under investigation. Based on experience in conventional tokamaks, it is likely that the scaling will become weaker as plasmas become less collisional [20]. The scaling with ν_e^* is particularly important because it is the dimensionless parameter that exhibits the biggest variation in extrapolating from present STs to an ST-based CTF.
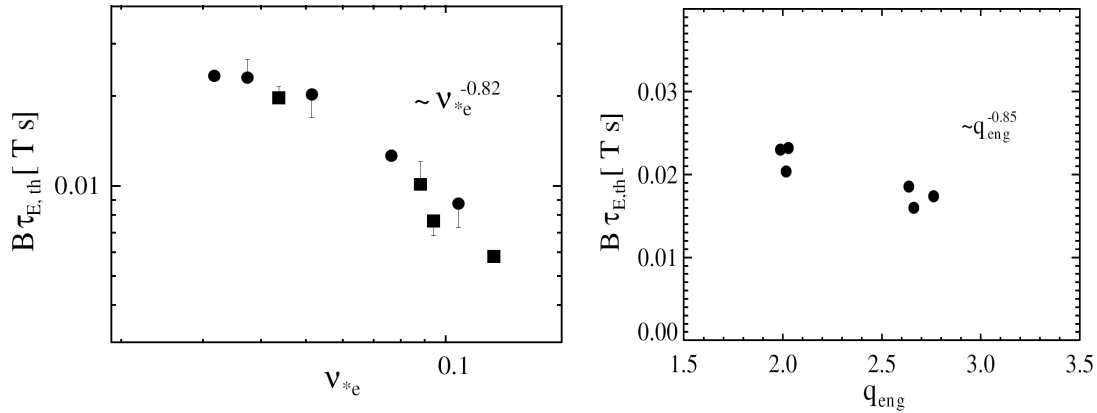

FIG. 2. Variation of thermal energy confinement time with electron collisionality and safety factor. Collisionality data are shown for two different plasma shapes ($\bullet$ $\kappa = 2.0$, $\blacksquare$ $\kappa = 1.7$)

3.2. Transport Studies

The availability of routine MSE data, together with further developments to Thomson scattering and charge exchange recombination spectroscopy (CXRS) systems, has enabled the
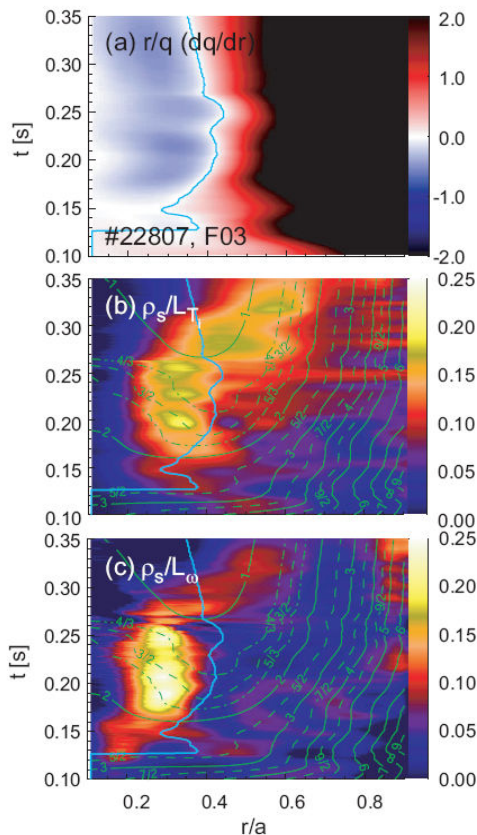

FIG. 3 Evolution of magnetic shear and normalized gradients of ion temperature and toroidal rotation for an L-mode discharge with co-NBI which forms an ITB. The blue contour denotes q_{min}.

influence of the q-profile and E×B flow shear on transport to be studied in MAST [21]. Shear flow suppression of anomalous transport plays an important role in determining the confinement properties of ST plasmas. Poloidal rotation is measured to be small in MAST, profiles being consistent with neoclassical predictions, and hence makes only a small contribution to the net E×B flow shear [22]. However, the strong toroidal rotation, driven by NBI heating, produces E×B shearing rates sufficient to exceed the growth rate of low-*k* ion-scale turbulence. In H-mode plasmas ion heat transport is within a factor 1-3 of the ion neo-classical level over most of the radius, while the electron transport remains highly anomalous. In L-mode plasmas, however, the ion transport can far exceed neo-classical levels in the outer regions but is strongly suppressed by flow shear at mid-radius and, under favourable conditions can exhibit an internal transport barrier (ITB) with ion transport at the neo-classical level. As in other tokamaks, ITB formation is favoured by early NBI heating of a low density L-mode discharge, applied during the current ramp to slow current penetration, resulting in strong toroidal rotation and reversed magnetic shear in the core. With co-NBI, ITBs in the momentum and ion thermal channels form in the negative shear region just

inside q_{min} (Fig. 3). Some correlation is found with the magnitude of the normalized toroidal rotation gradient and the passing of q_{min} through rational values. There is also evidence that anomalous fast-ion diffusion, driven by fast particle instabilities, may contribute to local enhancement of the E×B shearing rate. With counter-NBI, ITBs of greater radial extent form outside q_{min} due to the broader profile of E×B flow shear produced by the greater prompt fast-ion loss torque. The strength of ITBs in MAST is usually limited by coupling of MHD modes which reduce the rotation gradient and ultimately an internal kink mode (see section 2.1) removes the core flow shear destroying the ITB when q_0 approaches unity. Equilibrium flow shear has been included in gyro-kinetic codes (e.g. GS2), improving comparisons of linear and non-linear simulations with results from strongly rotating MAST plasmas [23]. Coupled multi-flux tube simulations (TRINITY) [24] and global simulations [25] (e.g. using the particle-in-cell code ORB5) with and without flow shear are also being pursued. For the discharge in Fig. 3, linear stability analysis with GS2 shows that all electrostatic micro-instabilities are stable in the negative magnetic shear region in the core, both with and without flow shear. Outside the ITB, in the region of positive magnetic shear and relatively weak flow shear, electrostatic micro-instabilities become unstable over a wide range of wave-numbers: at ITG length scales, flow shear reduces linear growth rates and narrows the spectrum of unstable modes, but flow shear suppression of ITG modes is incomplete; flow shear has little impact on growth rates at ETG scales. This is consistent with the observed anomalous electron and ion transport in this region. Non-linear ORB5 calculations indicate that T_i profiles may be clamped (i.e. 'stiff') by ITG turbulence outside the ITB region [25]. Measurements of the low-k turbulence in such ITB plasmas using a BES turbulence imaging system newly installed on MAST [26] will in future allow direct comparison of results from non-linear, ion scale turbulence simulations with observations in regions where low-k turbulence produces significant anomalous transport or is fully suppressed.

3.3. Pellet Fuelling

Fuelling and particle confinement investigations have focussed on 'shallow' pellet fuelling, where studies of pellet trajectory, ablation and post-pellet transport benefit from fast visible imaging and very high spatial and temporal resolution TS measurements, synchronised to the pellet propagation. Results have been compared with first principles ablation/deposition codes and confirm the importance of ∇B drift and plasma pre-cooling effects in determining the pellet penetration depth [27,28]. Furthermore, high spatial resolution visible bremsstrahlung imaging of the pellet trajectory reveals discrete structures, namely striations, that are related to the plasmoids which are responsible for re-deposition of pellet particles – the critical mechanism for ITER fuelling. The striations have a separation of $\sim 4-30$mm, which is comparable to the ion Larmor radius and indicates that finite Larmor radius effects may be important for pellet plasmoid dynamics [19]. The effectiveness of pellet refuelling of H-mode plasmas is also being studied in MAST, including compatibility with application of resonant magnetic perturbations (RMPs) for ELM control. The favourable effects of pellet injection for H-mode access and fuelling have been demonstrated.

4. Pedestal Physics & the L-H Transition

H-mode access and properties of the H-mode pedestal have an important influence on projected ITER performance. In recent MAST experiments, it has been shown that for helium discharges (with D beams) the H-mode power threshold, P_{LH}, is about 50% higher than for deuterium and, as observed in other devices, P_{LH} is reduced if the distance between the X-point and the strike point is shortened [29]. The sensitivity of H-mode access in MAST to magnetic geometry, especially close to DN, has been reported previously [30]. This sensitivity

may be exploited to control H-mode access [31] allowing, for example, very high resolution pedestal diagnostics to be synchronised to the H-mode transition. To elucidate the physical mechanisms underlying the L-H transition, which are not well-understood at present, the evolution of profiles of T_e, n_e and E_r at the transition have been measured with a time resolution $\Delta t < 200\mu s$ by Thomson scattering and edge Doppler spectroscopy [29]. Visible imaging shows that fluctuations are suppressed at the transition on a timescale $< 100\mu s$ whereas profile changes occur on a timescale at least 5 times slower, the density pedestal forming on a faster timescale than the temperature pedestal. Neither the gradient nor the mean values of T_e or E_r appear to play a major role in triggering the L-H transition.

Pedestal characteristics have been studied as a function of magnetic configuration and ELM type [32]. As for most other tokamaks, analysis of pedestal stability relies on calculations of the edge bootstrap current together with the assumption that $T_i = T_e$. Efforts are underway on MAST to improve pedestal stability analysis by direct measurement of these quantities [29]. First, a novel technique now provides high resolution T_i profiles in the pedestal [33]. T_i is deduced from the C^{6+} temperature using charge exchange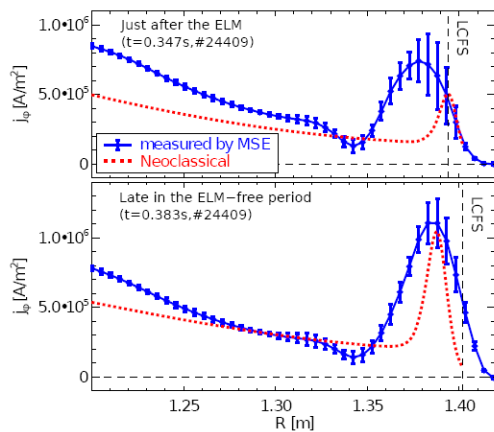 recombination of C^{6+} by excited D atoms. At high collisionality, the assumption $T_i = T_e$ is found to be a good approximation. However, at low collisionality, although $T_i \approx T_e$ at the top of the pedestal, the ion temperature gradient is much shallower than that of electron temperature so that $T_i > T_e$ further out. The data appear to be consistent with modified gyrokinetic theory [34] which requires $\rho_i^{pol}\nabla T_i \ll 1$ in the banana regime, where ρ_i^{pol} is the poloidal ion Larmor radius. Second, the evolution of the edge current density profile has been determined (with 2ms resolution) using MSE, a measurement made possible due to the large magnetic field pitch angle at the edge of an ST plasma [35]. Radial electric field corrections are included, from edge Doppler spectroscopy measurements, and are small. As expected, the measured edge current density in H-mode is significantly greater than that in L-mode. Measured H-mode current density profiles are compared with calculations of the neo-classical bootstrap current in Fig. 4, just after an ELM and later in the ELM free period. The calculated bootstrap current density appears to be somewhat smaller than that measured, with a narrower profile, the difference being more pronounced just after the ELM. At the time of the type I ELM, ELITE calculations show the discharge to be close to the ballooning stability boundary. Edge current density evolution may also be inferred from electron Bernstein wave emission. Initial measurements [36] indicate large variation in magnetic field line tilt angle over a very small region ($\leq$ 2cm) close to the LCFS, consistent with a local bi-directional radial current structure. Further investigations are planned using a new array of 36 antennas to image the electron Bernstein wave emission.

FIG. 4 Comparison of measured edge current density profiles (MSE) with those based on neo-classical bootstrap calculations.

5. ELM control

To avoid damage to in-vessel components in future devices such as ITER, a mechanism to reduce the size of type I ELMs is required. One such mechanism relies on perturbing the magnetic field in the edge plasma region, enhancing transport to keep the edge pressure gradient below the critical value that would trigger an ELM, while still maintaining an edge

transport barrier. This technique of Resonant Magnetic Perturbations (RMPs) has been successfully employed on DIII-D [37], where complete ELM suppression has been observed. A set of in-vessel ELM control coils consisting of two rows of six coils each, one above and one below the mid- plane, similar to the DIII-D I-coils, has been installed in MAST [38]. When n = 3 RMPs are applied to MAST L-mode discharges clear resonant effects are observed, namely density pump-out together with changes in edge fluctuation characteristics, in the edge radial electric field profile and in the perpendicular and parallel flows [39,40]. The pump-out is accompanied by a splitting of both the particle and heat flux to the divertor strike points, indicating that RMP penetration takes place [41]. The magnitude of the pump-out is correlated with the magnitude of the resonant component of the applied field rather than the width of the stochastic region produced at the edge of the plasma. The radial electric field profile flattens when the RMPs are applied, leading to an increase inside the separatrix and a decrease in the SOL. This change is consistent with what is expected from theories based on the establishment of a stochastic layer. Given that the pump-out and these other phenomena appear to require the same current threshold in the RMP coils, it seems likely that there is a modification of the turbulent transport level. This is in agreement with results from B2SOLPS modelling which show that the transport coefficients have to be increased in order to match the observed pump out and changes in electric field [42,43].

In H-mode plasmas just above the L-H transition threshold, the application of RMPs seems equivalent to a small decrease in input power. For example, more frequent ELMs can be triggered in a type III ELMing discharge and type III ELMs can be triggered in an ELM free discharge. In discharges with type I ELMs, little effect was observed initially, despite the fact that vacuum modelling (ERGOS) showed that the Chirikov parameter was greater than 1 over a wide radial extent, i.e. there was a wide stochastic region greater than that correlated with ELM suppression in DIII-D. However, following careful adjustment of q_{95} in these type I ELMing discharges, RMPs were observed to increase the ELM frequency (f_{ELM}) by a factor of 5 and decrease the energy loss per ELM (ΔW_{ELM}) from a mean value of ~5kJ to ~ 1kJ i.e. consistent with $\Delta W_{ELM} \cdot f_{ELM} \sim$ constant (Fig. 5). This effect on the ELMs is not correlated with the width of the region for w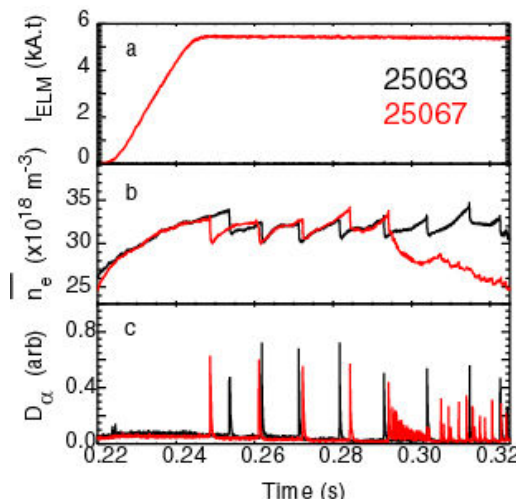hich the (vacuum field) Chirikov parameter is greater than 1 but may be correlated with the size of the resonant component of the applied field. Realistic modelling should include the response of the plasma to the RMP fields, in addition to the vacuum field produced by the coils. The *linear* and *nonlinear* response of the plasma to RMP fields, has been investigated using the MARS-F/K codes and the BOUT++ code, respectively [44]. The resonant spectrum of the vacuum field produced by the RMP coils is significantly modified near the edge of the plasma and the field amplitude near rational surfaces is significantly reduced. Calculations also show that rapid toroidal plasma rotation, as observed in MAST H-mode plasmas with type I ELMs, can provide efficient shielding. Since in ITER it will be necessary to suppress the first

FIG. 5 Mitigation of type I ELMs in MAST using n = 3 RMPs

large type I ELM, the RMPs may need to be applied before the L-H transition, which may affect the power required to access H-mode. On MAST the application of n=3 RMPs before the L-H transition can either suppress the L-H transition entirely or significantly delay it. For

the cases studied, it was necessary to increase the beam power by 30 - 40% to re-establish the L-H transition.

6. Exhaust Physics

6.1. Divertor Heat Load Studies & SOL Ti measurements

Quantification of heat loads (magnitude and spatial distribution) on plasma-facing components is important for the design of future devices as it impacts on component lifetime. Long-wave infrared (LWIR) and medium-wave infrared (MWIR) cameras have been used to measure heat load asymmetries (in/out and up/down) for a variety of magnetic configurations, with NBI power up to 3 MW [45]. As expected, the LWIR system is less sensitive to disturbances from hot spots or surface layers [46]. Good power accounting was obtained in L-mode discharges with ~ 100% of the power flowing to the SOL (radiation subtracted) reaching the divertor. The in/out asymmetry was found to be very sensitive to dr_{sep}, the distance between the two separatrices at the outboard mid-plane. In all cases, most of the energy arriving in the SOL goes to the outer divertor, confirming earlier probe data [47]. For double null (DN) discharges with $dr_{sep} \sim 0$, the observed ratio of power arriving at the outer strike-points to that at the inboard strike points lies in the range 20–40. Heat load asymmetries have also been studied during and between type-I ELMs for both DN and lower single null (SN) discharges. During DN discharges, most of the energy flows to the outer divertor and during ELMs, filamentary structures are observed at the outer divertor while the heat flux profile at the inner divertor remains largely unchanged. Although more energy arrives at the inner target in SN discharges, the largest amount of ELM energy is still deposited on the outer target and filamentary structures are observed at both the inner and outer divertors.

Langmuir probe data are widely used to infer energy fluxes to divertor and plasma facing components. The assumption $T_i = T_e$ is usually deployed to infer the electron density or power deposition from the probe data. Ion temperature measurements are important to reduce uncertainties in these derived parameters and because the energy of the ions determines the physical sputtering rates from plasma facing materials. Initial ion energy measurements have been obtained in the MAST outboard mid-plane SOL using a Retarding Field Analyzer (RFA) supplied by CEA Cadarache [48]. Example data are plotted in Fig. 6 for a beam heated lower SN L-mode discharge. The measurements in Fig. 6 are calculated to underestimate the unperturbed ion temperature by a factor 1 – 1.3 due to plasma flow effects. Accounting for this, it was concluded that for a range of L-mode discharges $T_i/T_e = 1 – 2.6$ in the MAST SOL. These results are quantitatively consistent with previous power balance studies in MAST [47] which showed that the total power calculated from Langmuir probe measurements at the divertor targets is equal to the power transported out of the confined plasma assuming $T_i = T_e$. Using the OSM2 transport model, this ratio can then be extrapolated to $T_i/T_e = 2 – 2.5$ at the mid-plane [49], in reasonable agreement with RFA measurements. First measurements have also been obtained in H-mode, with ion energies in excess of 500eV being detected 19cm away from the separatrix
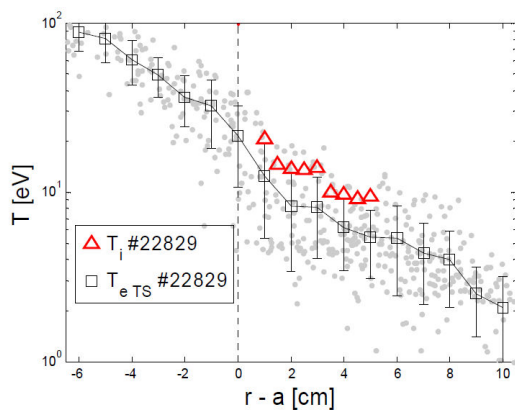

FIG. 6 Ion temperature profile measured by the retarding field analyzer (e-side) and electron temperature profile measured by TS in a beam heated lower single null L-mode plasma #22829 (I_p = 0.63MA, P_{NBI} = 2MW).

during saw-tooth triggered type-I ELMs.

Steady-state heat loads on plasma facing components may be reduced by operating with a 'detached' divertor, where plasma pressure and energy is dissipated along the divertor leg. Partial detachment can be achieved in MAST L-mode discharges (P_{NBI} = 1MW) with localized deuterium puffing into the lower inner divertor leg [50]. High resolution spectroscopic data from MAST will be used to constrain interpretive modelling efforts to ascertain the plasma conditions within the recombining region, and yield insights into the physical mechanisms that give rise to detachment.

6.2. Disruption Mitigation

Disruptions may lead to intolerable thermal and mechanical loads in future devices such as ITER. Hence they must be avoided or methods for mitigating their effects must be developed. MAST is equipped with a disruption mitigation system bas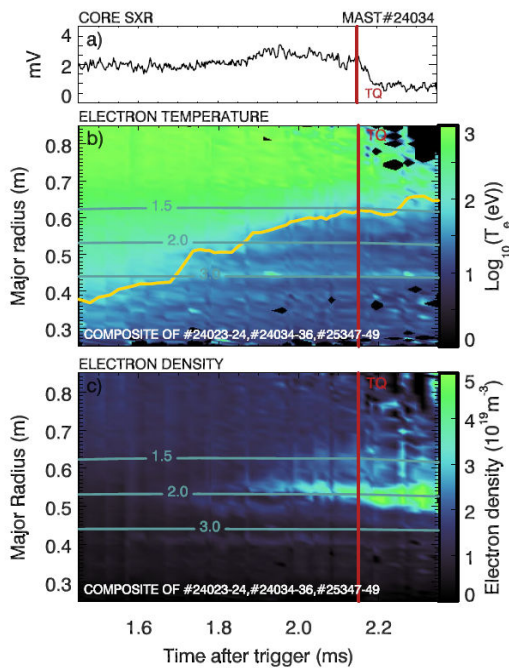ed on massive gas injection (fast gas valve supplied by FZ Jülich) which is capable of injecting up to 1.95 bar litres into the MAST vessel over a timescale of 1-2ms, corresponding to a particle inventory of 5×10^{22}, around 100 times the plasma particle inventory. In initial experiments, 0.4 bar-litres of a 10% argon, 90% helium mixture was injected [51]. High speed infrared thermography, offering full divertor coverage, has shown a 60-70% reduction in peak divertor power loads compared with unmitigated disruptions and a 55% reduction in divertor energy loads. Fast (20kHz) filtered imaging measurements show that the He impurity ions penetrate to the $q = 2$ surface prior to the thermal quench (TQ). The cooling caused by the injected gas leads to contraction of the current profile and destabilization of MHD activity coincident with the onset of the thermal quench. TS data show that the thermal quench is initiated after the cooling front has passed the $q = 2$ surface and after a significant density build up has taken place on the $q = 2$ surface (Fig. 7). During the thermal quench phase, impurity ion mixing with the bulk plasma occurs and the ion emission becomes increasingly distributed throughout the plasma volume.

FIG. 7 Mitigated disruption in MAST: a) soft X ray emission, b) electron temperature and c) density measured by TS on the inboard plasma side. $R_{mag-axis}$ = 0.9m. The locations of the q = 1.5, 2.0 and 3.0 surfaces are indicated. The temperature plot is logarithmic to highlight the T_e collapse.

6.3. Fuel Retention

Global particle balance has been used to investigate fuel retention in MAST [52]. Typically ≥ 80% of the injected particles are retained in the walls/divertor targets during each discharge; most of them are recovered during inter-shot [4]He Glow Discharge Cleaning (GDC). With inter-shot GDC to recondition the surfaces, retention does not saturate, whilst if there is no inter-shot GDC, the plasma density in subsequent discharges increases uncontrollably due to

the lower pumping capacity of the wall. Thus, on the relatively short time-scale of MAST pulses, it appears that the particle balance is dominated by direct implantation of ions and neutrals in shallow surface layers.

6.4. Dust studies

Quantities of dust must be carefully controlled in fusion devices. Dust samples have been collected from MAST to identify their shape, structure, chemical composition and distribution [53]. Stereoscopic imaging of dust particle motion in both the divertor and main chamber, using fast infra-red and visible cameras [54] has allowed the 3D trajectories of the particles to be reconstructed. During disruptions (vertical displacement events) an isotropic release of dust particles from the plasma facing surfaces is observed with velocities up to $350m.s^{-1}$. Stereoscopic imaging has also been used, for the first time, to study the mobilization and transport of carbon and tungsten particles with known size distributions which were introduced into the lower divertor plasma through the Divertor Science Facility. For carbon particles a correlation between the particle size and acceleration by the plasma is observed. For tungsten particles the initial velocities are found to be lower and the particles experience lower acceleration by the plasma. On the other hand, tungsten particles are found to be more prone to vertical motion towards the core plasma, leading to early disruptions for large particles. Dust injection experiments have been modelled using the DTOKS code [55] in an attempt to validate the transport equations employed. Initial simulations confirm the different behaviour of carbon and tungsten particles and are able to reproduce the observed velocity range and acceleration [54].

7. Future Plans

New capabilities that will be available in 2011 include additional ELM control coils, a 2D beam emission spectroscopy system, a fast ion D_α system (FIDA), a 4-chord collimated neutron detector, an electron Bernstein wave imaging system, new retarding field energy analyzers and improvements to the edge Doppler spectroscopy system enabling high frequency fluctuation measurements ($\geq$ 50kHz). These developments will significantly enhance our capabilities to study ELM control, turbulent transport, fast ion behaviour and pedestal physics. In the longer term, an upgrade to MAST (MAST-U) has been designed and the first major stage is now to be implemented [56]. The initial upgrade will incorporate and test a closed cryo-pumped divertor configuration based on the super-X concept [57] and enable assessment of dominantly non-inductive operation at the $I_p \geq$ 1MA level for several current diffusion times. A new centre column and toroidal field power supply will give increased solenoid flux and toroidal magnetic field whilst new poloidal field coils will allow increased plasma shaping. The NBI power will be raised initially to 7.5MW, with increased off-axis current drive capability. Together these improvements will significantly extend the operating space of MAST, particularly towards lower normalized collisionality. This should enable substantial progress on the most critical physics issues for an ST-based CTF and further strengthen MAST contributions to ITER- and DEMO-relevant physics.

References

[1] I.T. CHAPMAN et al, 23rd IAEA Fusion Energy Conference 2010, Paper EXS/P5-04
[2] I.T. CHAPMAN et al, Nuc. Fus. **50** (2010) 045007

[3] I.T. CHAPMAN *et al,* Nuc. Fus. **50** (2010) 025018
[4] C. WAHLBERG *et al,* Phys. Plasmas **16** (2009) 112512
[5] M-D. HUA *et al,* Plasma Phys. Control. Fusion **52** (2010) 035009
[6] K.J. GIBSON *et al,* Plasma Phys. Control. Fusion (2010), submitted
[7] I.T. CHAPMAN *et al,* Phys. Rev. Lett., in preparation
[8] M.R. TURNYANSKIY *et al,* Nuc. Fus. **49** (2009) 065002
[9] M.R. TURNYANSKIY *et al,* Proc. 36th EPS Conf. 2009
[10] M. CECCONELLO *et al,* Rev. Sci. Instrum., accepted
[11] I. JENKINS *et al,* Proc. 37th EPS Conf. 2010
[12] M.K. LILLEY *et al,* 23rd IAEA Fusion Energy Conference 2010, Paper EXW/P7-14
[13] M.K. LILLEY *et al,* Phys. Rev. Lett. **102** (2009) 195003
[14] M.K. LILLEY *et al,* Phys. Plasmas (2010) accepted
[15] S.D. PINCHES *et al,* Comp. Fus. Comm. **111** (1998) 133
[16] G.M. VOSS *et al,* Fus. Eng. & Des. **83** (2008) 1648
[17] M. VALOVIC *et al,* Nuc. Fus. **49** (2009) 075016
[18] S.M. KAYE *et al,* Nuc. Fus. **47** (2007) 499
[19] M. VALOVIC *et al,* 23rd IAEA Fusion Energy Conference 2010, Paper EXC/P8-18
[20] T.C. LUCE *et a*l, Plasma Phys. Control. Fusion **50** (2008) 043001
[21] A.R. FIELD *et al,* 23rd IAEA Fusion Energy Conference 2010, Paper EXC/P8-04
[22] A.R. FIELD *et al,* Plasma Phys. Control. Fusion **51** (2009) 105002
[23] C. ROACH *et al,* Plasma Phys. Control. Fusion **51** (2009) 124020
[24] M. BARNES *et al,* 23rd IAEA Fusion Energy Conference 2010, Paper THC/P4-01
[25] S. SAARELMA *et al,* Proc. 37th EPS Conf. 2010
[26] A.R. FIELD *et al,* Rev . Sci. Instrum. **80** (2009) 073503
[27] M. VALOVIC *et al,* Nuc. Fus. **48** (2008) 075006
[28] L. GARZOTTI *et al,* Nuc. Fus. **50** (2010) 105002
[29] H. MEYER *et al,* 23rd IAEA Fusion Energy Conference 2010, Paper EXC/2-3Ra
[30] H. MEYER *et al,* Plasma Phys. Control. Fusion **47** (2005) 843
[31] H. MEYER *et al,* Plasma Phys. Control. Fusion **50** (2008) 015005
[32] A. KIRK *et al,* Plasma Phys. Control. Fusion **51** (2009) 065016
[33] T.W. MORGAN *et al,* Proc. 37th EPS Conf. 2010
[34] G. KAGAN & P.J. CATTO, Plasma Phys. Control. Fusion **50** (2008) 085010
[35] M. DeBOCK *et al,* Proc. 37th EPS Conf. 2010
[36] V.F. SHEVCHENKO *et al,* Fusion Science & Technology, accepted
[37] T. EVANS *et al,* Phys. Rev. Lett. **92 (**2004) 235003
[38] A. KIRK *et al,* Nuc. Fus. **50** (2010) 034008
[39] A. KIRK *et al,* 23rd IAEA Fusion Energy Conference 2010, Paper EXD/8-2
[40] P. TAMAIN *et al,* Plasma Phys. Control. Fusion **52** (2010) 075017
[41] E. NARDON *et al,* Plasma Phys. Control. Fusion **51** (2009) 124010
[42] V. ROZHANSKY *et al,* Nuc. Fus. **50** (2010) 034005
[43] V. ROZHANSKY *et al,* 23rd IAEA Fusion Energy Conference 2010
[44] Y. LIU *et al,* 23rd IAEA Fusion Energy Conference 2010, Paper THS/P5-10
[45] G. De TEMMERMAN *et al,* Plasma Phys. Control. Fusion **52** (2010) 095005
[46] E. DELCHAMBRE *et al,* Plasma Phys. Control. Fusion **51** (2009) 055012
[47] A. KIRK *et al,* Plasma Phys. Control. Fusion **46** (2004) 551
[48] P. TAMAIN *et al,* J. Nucl. Mater., accepted
[49] A. KIRK *et al,* Plasma Phys. Control. Fusion **46** (2004) 1591
[50] J. HARRISON *et al,* J. Nucl. Mater., submitted
[51] A. THORNTON *et al,* J. Nucl. Mater., submitted
[52] J. HUANG *et al,* Plasma Phys. Control. Fusion **52** (2010) 075012
[53] C. ARNAS *et al,* J. Nucl. Mater. **401** (2010) 130
[54] G. De TEMMERMAN *et al,* Nuc. Fus. **50** (2010) 105012
[55] M. BACHARIS *et al,* Phys. Plasmas **17** (2010) 042505
[56] D. STORK *et al,* 23rd IAEA Fusion Energy Conference 2010
[57] M. KOTSCHENREUTHER *et al,* Phys. Plasmas **14** (2007) 072502